Aleisa, H., Kontis, K. and Nikbay, M. (2023) Numerical investigations on low-speed aerodynamic characteristics of generic unmanned combat aerial vehicle configurations. *Journal of Aircraft*, 60(6), pp. 1832-1846 (doi: 10.2514/1.C037258)

There may be differences between this version and the published version. You are advised to consult the published version if you wish to cite from it.
https://doi.org/10.2514/1.C037258

http://eprints.gla.ac.uk/297127/

Deposited on 26 April 2023

Enlighten – Research publications by members of the University of Glasgow
http://eprints.gla.ac.uk

Numerical Investigations on Low-Speed Aerodynamic Characteristics of Generic UCAV Configurations

Hassan Aleisa* and Konstantinos Kontis†
University of Glasgow, Glasgow, G12 8QQ, UK

Melike Nikbay‡
Istanbul Technical University, Istanbul, 34469, Türkiye

The leading-edge sweep angle significantly influences the flight performance of swept wings. The vortex flow structures affect the flow behavior of the moderate to highly swept wings, which form at low angles of attack because of leading-edge flow separation. This topic of investigation recently gained momentum due to its application to unmanned combat aerial vehicle (UCAV) configurations that are significantly affected by flow separation at high angles of attack. The present work investigates the flowfield and low-speed aerodynamic characteristics of the generic UCAV models with a constant and non-constant leading-edge sweep for a wide range of angles of attack. The open-source computational fluid dynamics (CFD) code OpenFOAM 8.0 is employed for the numerical simulations. The present numerical simulation results agree well with the experimental data in the literature. It is demonstrated that the lift and drag characteristics of the UCAV are sensitive to the leading-edge sweep angle, and a non-constant leading-edge sweep angle variant exhibits delayed stall and enhanced aerodynamic performance.

Nomenclature

AOA	=	angle of attack [^{o}]
AR	=	wing aspect ratio [-]
b	=	wingspan [m]
C	=	chord [m]
C_D	=	wing drag coefficient [-]
C_L	=	wing lift coefficient [-]
C_P	=	pressure coefficient [-]
LE	=	leading edge [-]
P	=	pressure [N/m^2]

*Postgraduate Research, Aerospace Engineering Department, AIAA Member.
†Professor, Aerospace Engineering Department, AIAA Fellow
‡Professor, Faculty of Aeronautics and Astronautics, Astronautical Engineering Department, AIAA Associate Fellow

PS	=	pressure surface [-]
SS	=	suction surface [-]
TE	=	trailing edge [-]
U	=	free-stream velocity [m/s]
u	=	local velocity [m/s]
X, Y, Z	=	coordinate axes
X	=	chordwise direction [m]
Y	=	spanwise direction [m]
Z	=	vertical direction [m]
$Y+$	=	non-dimensional wall distance [-]
Λ	=	sweep angle [^{o}]
k	=	turbulence kinetic energy [m^2/s^2]
ω	=	specific turbulence dissipation rate [1/s]
CFD	=	computational fluid dynamics
$UCAV$	=	unmanned combat aerial vehicle

Subscripts

D	=	drag
L	=	lift
P	=	pressure
LEI	=	leading edge inboard
LEO	=	leading edge outboard
TE	=	trailing edge

I. Introduction

THE performance and maneuverability of UCAVs are heavily reliant on the aerodynamic characteristics of the swept tailless flying wing at medium to higher AOA. A conventional two-dimensional (2-D) airfoil's stall angle is roughly 10-15°; however, flying wing types, including delta, diamond, and lambda wing configurations, can increase UCAV aerodynamic performance at greater AOA values. On the other hand, the benefits of swept flying wing vortices are limited; at a greater AOA, vortex breakdowns result in an abrupt drop in lift owing to stalling.

In 1931, Alexander Lippisch initially developed a delta wing configuration in Germany. Darmstadt München-1 (DM-1) was created to research low-speed aerodynamics. However, the thick and blunt edges of the DM-1 glider design reduced the critical AOA and lift coefficient. A sharp LE strip was integrated into the 60° swept wing DM-1 glider,

causing a vortex flow over the wing SS and delaying the stall point to a higher AOA [1]. Haines [2] compared the low-speed flow behavior around swept wings with a simple design. Furthermore, comparisons were made between the flow around a 2-D airfoil and the flow around swept wings. According to the report, AOA, Reynolds number, and wing configuration alter the area of detached flow and their related part-span vortex sheets. The flow physics of LE vortices and vortex flow separation at 65° delta wing with sharp LE were investigated by wind tunnel experiments of Lambourne and Bryer [3]. They demonstrated the vortex breakdown using oil-flow patterns and concluded that the adverse pressure gradient significantly influences the vortex breakdown along with the vortex [4]. Earnshaw [5] studied the vortex pair on a delta wing experimentally and found that a sharp-edged delta wing produced a primary vortex that could be classified as a viscous sub-core, rotating core, or free shear layer. Earnshaw and Lawford [6][7] conducted some studies on the effect of sweep angles on the flow over delta wings with sweep angles of 65° and 70°. Polhamus [8] provided an analytical model based on the LE suction analogy to calculate the vortex lift of sharp-edged delta wings. For a higher AOA value ($\approx 20^o$), it produced a better prediction of total lift.

At critical angles of incidence, these types of swept wings are subjected to LE separation, characterized by complex localized three-dimensional (3-D) vortical flow topologies such as separation structures or separation bubbles. The 3-D vortical flow is more complicated than the 2-D case; thus, the description of 3-D separated flows is challenging in many considerations. Various authors have made substantial contributions in reporting the flow field, in which 3-D separation effects occur significantly [9–11]. Furthermore, many studies have been conducted to analyze the vortex flow of delta wings using wind tunnel experiments and CFD [12–18]. These studies investigated the aerodynamic characteristics of wings with constant aspect ratio, LE sweep angles, and varied LE contours.

For a non-slender delta wing with a $\Lambda_{LE} \leq 55^o$ [14, 16] a distinct dual primary vortex structure with the same sense of rotation at high AOA occurs and results in complex interactions with the secondary vortical structure and wingtip structures [16]. In addition, the vortex flow behavior on a sharp LE non-slender delta wing varies significantly from the vortical flow on a slender delta wing [17]. For the sharp LE slender delta wing $\Lambda_{LE} > 55^o$, the primary flow detachment occurs at the sharp LE, and the detached flow rolls up to form a primary LE vortex [18]. A suction peak is generated due to the spanwise flow over the wing SS which is induced by the primary vortical flow. Following this suction peak, the unfavorable spanwise pressure gradient detaches the spanwise boundary layer flow, causing a secondary flow detachment and a secondary vortical flow. This secondary vortical flow prompts a suction outboard of the primary vortical flow suction peak [18]. These fundamental studies improved the understanding of delta wing aerodynamics and the investigations related to UCAV configurations (Fig.1). Also, the flying wings with a non-constant sweep angle and different TE configurations provide distinguished flow behavior characteristics compared to a basic delta wing configuration.

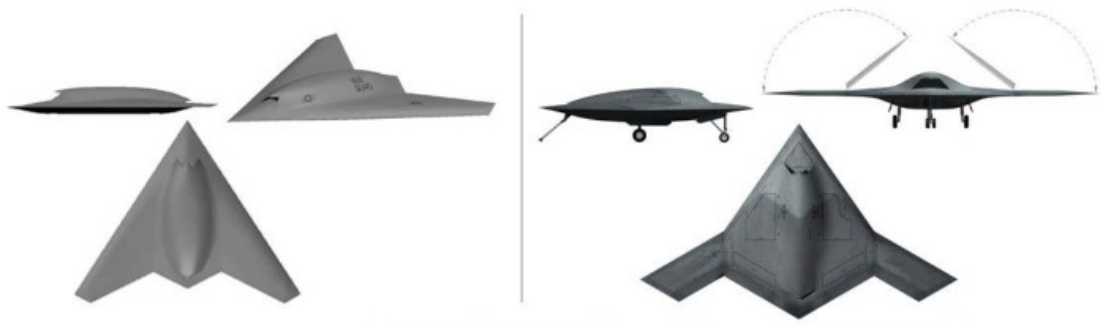

Fig. 1 Boeing X-45C (left) and Northrop Grumman X-47B (right) demonstrators [19].

The focus of vortex flow investigations has been increasingly placed on variable planform parameters for lambda wings to design wing configurations with reduced wing sweeps and swept TE. The lambda wings with sharp and rounded LE geometry were designed particularly for UCAVs to achieve the essential requirements. Many experimental and numerical studies were performed on UCAV lambda wing models such as UCAV 1303 (Λ_{LE} = ±47°, Λ_{TE} = ±30°) [20–25], Stability And Control CONfiguration (SACCON) (Λ_{LE} = ±53°, Λ_{TE} = ±53°) [26–34] and MULti DIsciplinary CONfiguration (MULDICON) (Λ_{LE} = ±53°, Λ_{TE} = ±30°) [34–38] to understand their aerodynamics characteristics. These configurations represent constant LE sweep UCAV configurations such as Boeing X-45C Phantom Ray, Northrop Grumman X-47A Pegasus, Dassault nEUROn, and BAE Taranis. Konrath et al. [27] examined the flow structure over a 53° LE sweep lambda wing. Various vortex systems such as apex vortical flow, a LE vortex, and a thickness-caused vortex were observed [27]. The vortex intensity, turbulent kinetic energy, and velocity oscillations near the surface rise as the AOA increased [31].

Flows over wings with moderate sweep angle, typically from 30-50° [39], have received increased investigations due to their use in UCAV for military applications. However, the constant LE with low to moderated sweep angle configurations tends to cause advanced stall because of vortex breakdown. To overcome this shortcoming, appropriate sweep angles for the inboard and outboard planes were adopted in designs such as Boeing X-45A/B (Λ_{LEI} = ±45°,Λ_{LEO} = ±45°, Λ_{TE} = ±45°), and Northrop Grumman X-47B (Λ_{LEI} = ±55°,Λ_{LEO} = ±30°, Λ_{TE} = ±30°) [18, 40, 41].

Manshadi et al. [42] studied the flow field for a planform similar to Northrop Grumman X-47B aircraft at low speeds. They carried out velocity and pressure measurements for sharp LE and round LE in various cross planes on the wing SS of the model. They concluded that the sharp LE produced relatively high strength vortices compared to the round LE case. Additionally, Yaniktepe et al. [43] performed an experimental study on X-45 A/B configuration to analyze the effects of AOA on flow structure. They found that the X-45 A/B planform wing has superior lift characteristics compared to the generic delta wing with a sweep angle of 60°.

Based on the above discussion, it is evident that the LE sweep angle is a critical parameter that affects the aerodynamic performance of UCAV wings. Furthermore, the performance, signature, and weight considerations of

the real UCAVs often result in adopting planforms with swept edge-aligned of ($40^o \leq \Lambda \leq 60^o$) [25, 44–46] with associated medium aspect ratios, which are adequate to induce LE vortex separations during the maneuver, nevertheless less than conventional slender wing values [40]. However, the UCAVs must operate in complex conditions and expand their maneuvering envelope to higher AOA. For example, some of these UCAVs are required to takeoff and land on aircraft carriers, and they interact with the air ship wake during their landing on the carrier. UCAVs are subjected to complex mixed attached/separated flow fields at high lift conditions. The X-47B was the first UCAV to successfully takeoff and land for carrier-based operations [41].

Almost all the previous investigations related to UCAV configurations were focused on the aerodynamic performance and flow physics of planforms such as delta, cranked delta, double delta wing, and constant LE sweep angles lambda wings such as 1303, SACCON, and MULDICON. However, non-constant LE sweep angle lambda wing configuration, such as the X47-B, has been developed, but research data is rarely available on this planform. Hence, the novel wing planform like the X-47B configuration is considered to characterize the conditions of takeoff and landing of UCAVs.

The conceptual design of UCAVs is close to conventional attacker aircraft, and they can be developed between the bomber and the fighter [47]. Hence, in this study, two planforms have been considered. The first planform is a flying wing (lambda) with a 40° LE sweep angle close to the planform characteristics of a flying wing bomber. The second planform is a flying wing (lambda) with a $60/40^o$ LE sweep angle, considering the planform characteristics of fighters.

The present work aims to study the combined effect of a higher and moderate sweep angle ($60/40^o$ delta-lambda wing) on the vortex flow structure and compare it with a moderate sweep angle case (40° lambda wing). The present investigation also discusses the effect of constant and non-constant LE sweep angle on the vortex development, its strength, the location of the flow separation, and vortex breakdown. The flow field analyses of the wing models are presented and explained using the post-processed figures.

II. Model Geometry

Two flat plate lambda models with leeward beveled LE are used in the present study are shown in Fig.2. The wing models have identical dimensions except for the root chord length and LE sweep angle.

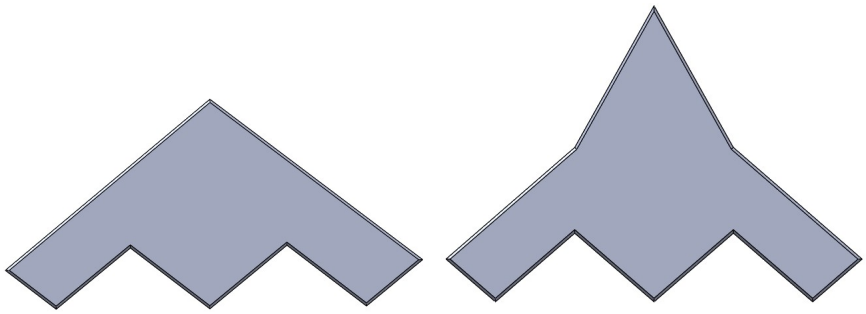

Fig. 2 Top view of Model 1 (left) and Model 2 (right) lambda wings.

The geometrical characteristics of the wing models (Model 1 and Model 2) utilized in the numerical analyses are listed in Table.1.

Table 1 Geometrical parameters

Parameters	Model 1	Model 2
LE inboard sweep angle, $\Lambda_{LEI}[^o]$	40	60
LE outboard sweep angle, $\Lambda_{LEO}[^o]$	-	40
TE sweep angle, $\Lambda_{TE}[^o]$	40	40
Wing area, S [m^2]	0.145	0.15
Wing span, b [m]	0.75	0.75
Root chord, C_r [m]	0.40	0.52
Mean Aerodynamic Chord, C_{mac} [m]	0.22	0.36
Wing thickness, t [m]	0.006	0.006
Bevel angle [^{o}]	45	45

III. Computational Methodology

A. Flow Domain and Boundary Conditions

Fig.3 displays the computational flow domain for the numerical analyses. The half-span of the model with a symmetry plane was employed to take advantage of the symmetrical nature of the wing model. The upstream and downstream distances were fixed as 2.4 m, and 5.4 m, respectively, and the domain was extended 2.4 m in the spanwise direction. The walls were placed away from the wing model and provided with slip wall boundary conditions, whereas the lambda wing model was kept as a no-slip wall.

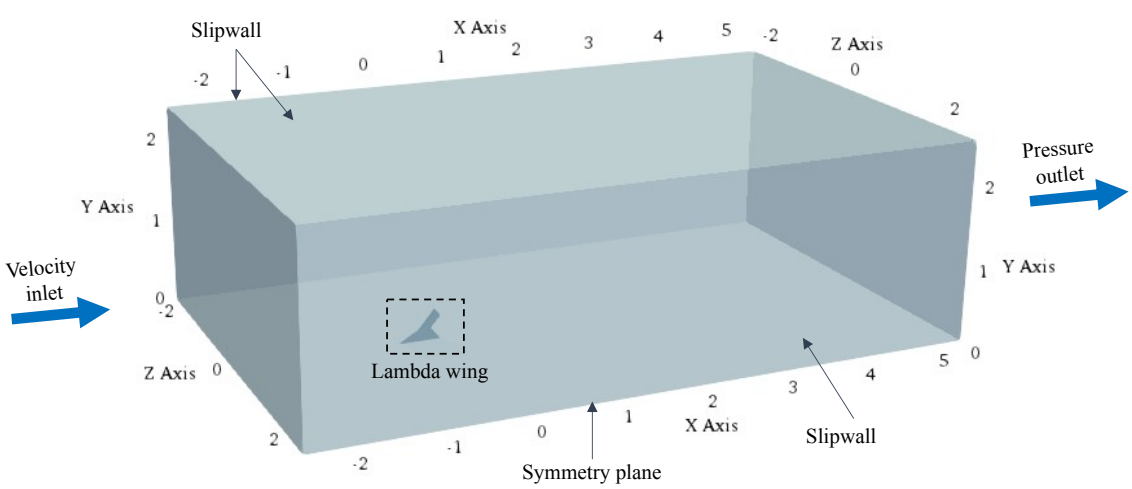

Fig. 3 Computational flow domain.

The wing models were rotated in the Y-axis to get the AOA values 0-40° with the step of 5°, while the flow domain

remained unchanged. The models are created using SolidWorks [48] and exported to a mesh generator as Standard for the Exchange of Product Data (STEP) and Stereolithography (STL) formats. A uniform axial velocity of 32 m/s with a low turbulence intensity of I = 1% was used at the inlet. Also, an estimate for the viscosity ratio was $\mu_t/\mu = 2$. A zero-pressure gradient condition was imposed at the outlet.

B. Grid Generation

In the present study, the inbuilt OpenFOAM [49, 50] grid generators, namely blockMesh + snappyHexMesh, are used to discretize the flow domain with 2 to 6 million cells mesh sizes (Fig.4 and Fig.5). The snappyHexMesh generates a 3D mesh from a triangulated surface geometry in STL format, incorporating hexahedral, polyhedral, and prism cells. In order to create a better mesh, the snappyHexMesh offers several options to enhance the edges, surfaces, and volumes. The blockMesh is used to produce the structured background mesh for the snappyHexMesh. In addition, the snappyHexMesh requires STL files that were exported from the Salome 2019 pre-processing package [51]. The STL files were placed on the triSurface folder and were used to carve out the geometry from the background mesh.

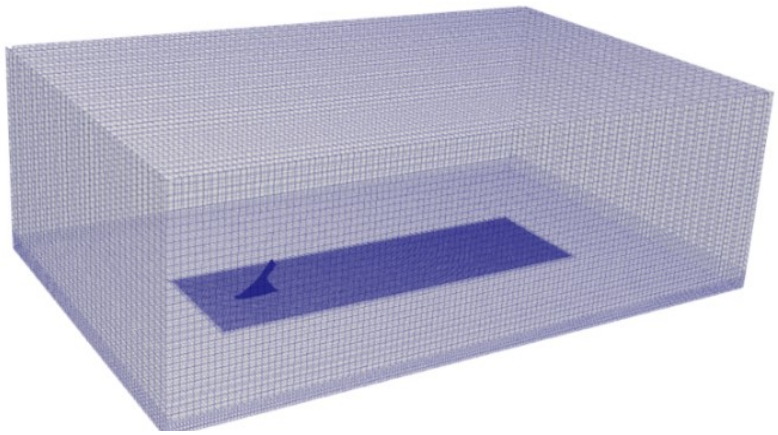

Fig. 4 3D view of meshed domain.

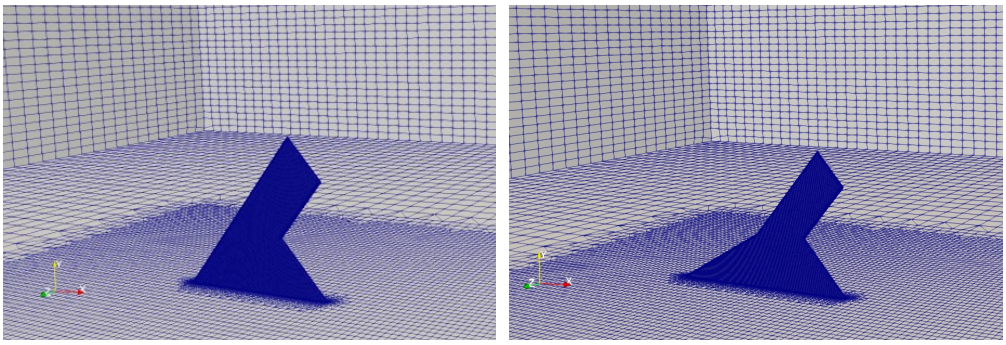

Fig. 5 SnappyHexMesh for the 40° (left) and 60/40° (right) lambda wings.

After the generation of mesh, its quality was verified using the checkMesh command. The critical parameters such

as aspect ratio, skewness and non-orthogonality were assessed and provided in Table 2. As shown in the table, the values of the parameters are within the acceptable range and the same mesh parameters were retained for all configurations used in this study. Moreover, to maintain the y+ $\leq$ 1, we generated 15 prism layers on the wing model with a layer growth ratio of 1.05 (Fig.6). The snappyHexMesh has an inherent limitation, such as the prism layers breakdown near the sharp edges, which increases the local y+ value in that region. Several authors who chose snappyHexMesh as their grid generator ran into a similar issue [52].

Table 2 Parameters of mesh quality

Parameter	Model 1	Model 2
Maximum aspect ratio [-]	5.31	4.45
Maximum skewness [-]	4.69	3.25
Maximum non-orthogonality [^{o}]	63.97	64.90
Average non-orthogonality [^{o}]	6.89	11.90

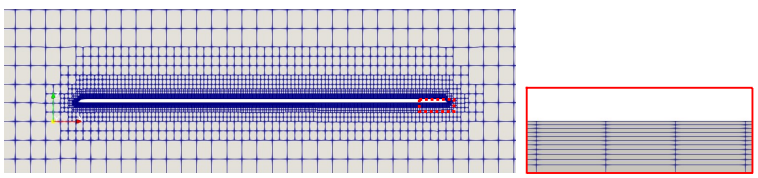

Fig. 6 The surface mesh of wing models at the symmetry plane.

Fig. 7 shows the SS y+ distribution for the two wing models. As shown in the figure, the value of y+ lies between 0 to 0.80 for both cases. As explained earlier, the maximum value of y+ occurs near the sharp edges; however, the average y+ value of the models is <1. Hence, we can conclude that the present mesh is adequate to solve the boundary layer of the studied wing models.

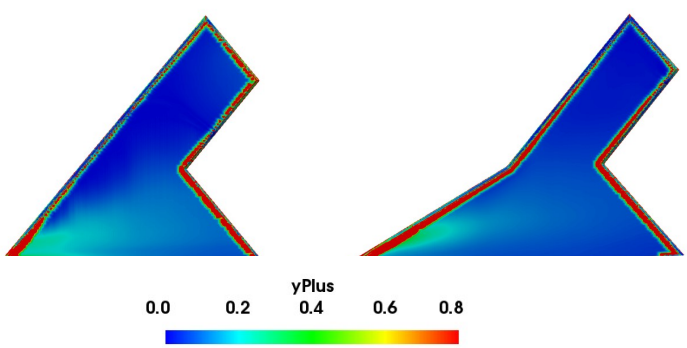

Fig. 7 SS y+ distribution for the 40° (left) and 60/40° (right) lambda wings.

C. Solver and Turbulence Model Selection

The flow over the UCAV at higher angle of attack exhibit high unsteadiness due to vortex breakdown, however the objective of the present study is to compute the aerodynamic performance of the UCAV model and not to investigate the complex vortex breakdown mechanism. It is noteworthy to mention Yavuz [53] established that the steady and mean unsteady results exhibit marginal variation compared to the experiments. Moreover, the vortex location and rotation are similar for both RANS and URANS solutions [15, 53–56]. Furthermore, k-w SST performs better in capturing the vortex breakdown with minimal computational time [57]. Hence, the present study used RANS approach to compute the aerodynamic performance.

The OpenFOAM offers various solvers [49, 50], and based on the present problem definition, the simpleFOAM solver is selected for the analysis suitable for the steady and incompressible flow. Regarding the turbulence model, the present study uses the k-ω shear stress transport (SST) model, which is suitable for flows with separation. It is a hybrid model that uses k-ω in the region closer to the wall and k-ϵ in the region away from it. Moreover, accurate second-order schemes are used for the spatial discretization, and the under-relaxation factors used in this study are 0.3 for pressure and 0.70 for all other variables. Numerous studies have effectively applied the k-ω SST model to determine the aerodynamic characteristics of tailless flying wing models [21, 58–63].

IV. Results and Discussion

A. Grid Independence Study

The grid convergence index (GCI) is used to evaluate the effect of grid resolution on the aerodynamic characteristics of the 40° lambda (Model 1) and the $60/40^o$ lambda (Model 2) wings. Three grids such as coarse, medium, and fine are generated, and their lift to drag ratio (C_L/C_D) values at 20° AOA are compared. The GCI is computed based on the approach provided by Celik et al [64], as shown in Table 3. The C_L/C_D values at 20° AOA for the 40° lambda and the $65/40^o$ lambda wings for various grids are shown in Fig.8.

Table 3 Numerical uncertainty assessment

Parameter		Model 1	Model 2
Number of elements (million)	Fine, medium and coarse	6.090, 4.471, 2.840	6.132, 4.370, 2.919
Average cell size	h_1,h_2,h_3	0.00547, 0.00607, 0.00706	0.00546, 0.00611, 0.00699
Grid refinement factor	r_{21},r_{32}	1.1085, 1.1633	1.1195, 1.1440
Performance parameter	ϕ_1, ϕ_2, ϕ_3	2.8486, 2.8427, 2.8397	2.8405, 2.8303, 2.8255
Apparent order	p	6.8738	6.5383
Approximate relative error	e_a^{21}, e_a^{32}	0.00103, 0.00209	0.00171, 0.00358
Extrapolated values	$\phi_{ext}^{21}, \phi_{ext}^{32}$	2.8369, 2.8394	2.82106, 2.82316
Extrapolated relative error	$e_{ext}^{21}, e_{ext}^{32}$	0.001001, 0.001145	0.00157, 0.00254
GCI	GCI_{fine}^{21},GCI_{medium}^{32}	0.001250, 0.001430	0.00196, 0.00317

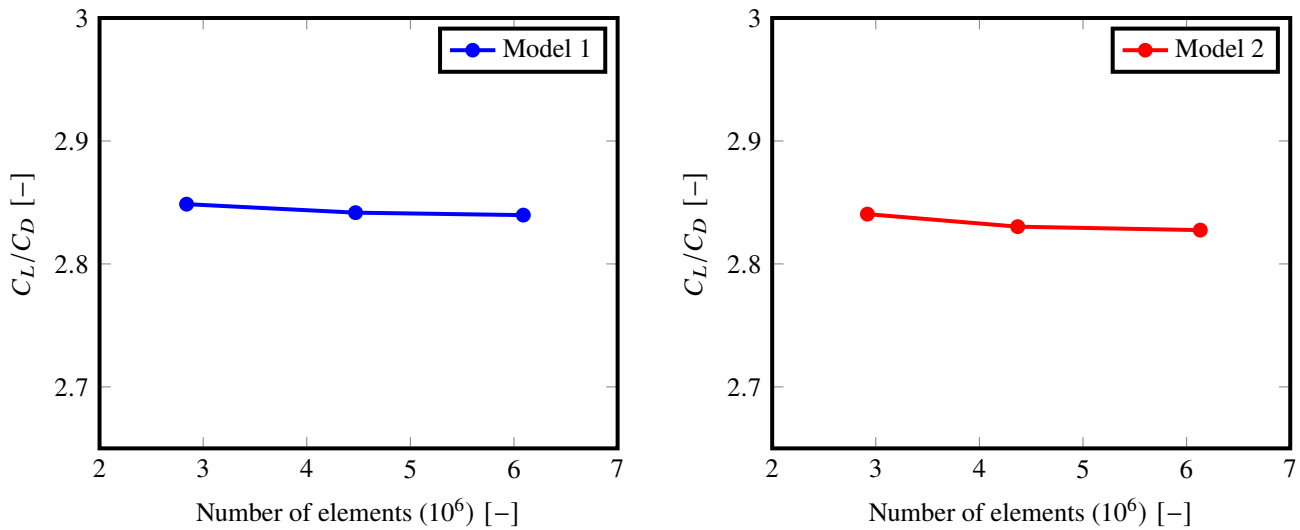

Fig. 8 Comparison of C_L/C_D values at AOA=20° for various grids.

For the 40° lambda wing, the GCI and the e^{32}_{ext} are about 0.14 and 0.11%, respectively, for the medium grid. Likewise, for the fine grid, the values are 0.12 and 0.10%, respectively. It can be observed that uncertainty due to spatial discretization reduces with increase in the grid resolution. On the other hand, a similar trend is observed for the 60/40° lambda wing. The variation between the GCI of medium and fine grids are insignificant. Furthermore, the GCI between the coarse and medium grids are less than 2% and the spatial grid convergence was attained as the GCI between the progressively refined grids are lower than 3% [65, 66]. Hence, as a trade-off between the accuracy and the computational time, the present study retained the medium grid for the numerical analysis to reduce the computational cost for the simulations.

B. Validation

The present study examines the aerodynamic characteristics of constant and non-constant LE sweep angle lambda wing configurations using OpenFOAM for various AOA. The parameters such as coefficients of lift (C_L), drag (C_D) and pitching moments (C_M) are compared with the experimental data of Ali and Chadwick for validation [45]. Fig. 9 compares the current study's computational results of C_L, C_D and C_M for 40° and 60/40° lambda wing models with the experimental data from the literature. The results of C_L, C_D and C_M are compared against the AOA ranging from 0 to 40°. As apparent in the plot, with an increase in AOA, the C_L increases up to a certain AOA and then stalls, reducing the lift. In contrast, C_D increases with AOA because the area resisting the airflow increases. The computational values of C_L and C_D agree well with the experimental data for the entire flow range. The critical stall points of the 40° and 60/40° lambda wings are approximately 20° and 30°, respectively. Moreover, as shown in the C_M plot moment coefficient reduces with an increase in AOA, and they exhibit a larger deviation from experimental data at higher AOA.

A similar behavior was observed in the study of Ali and Chadwick [45]. Hence, it can be concluded that the present numerical model is sufficient to study the aerodynamic performance of lambda wing models.

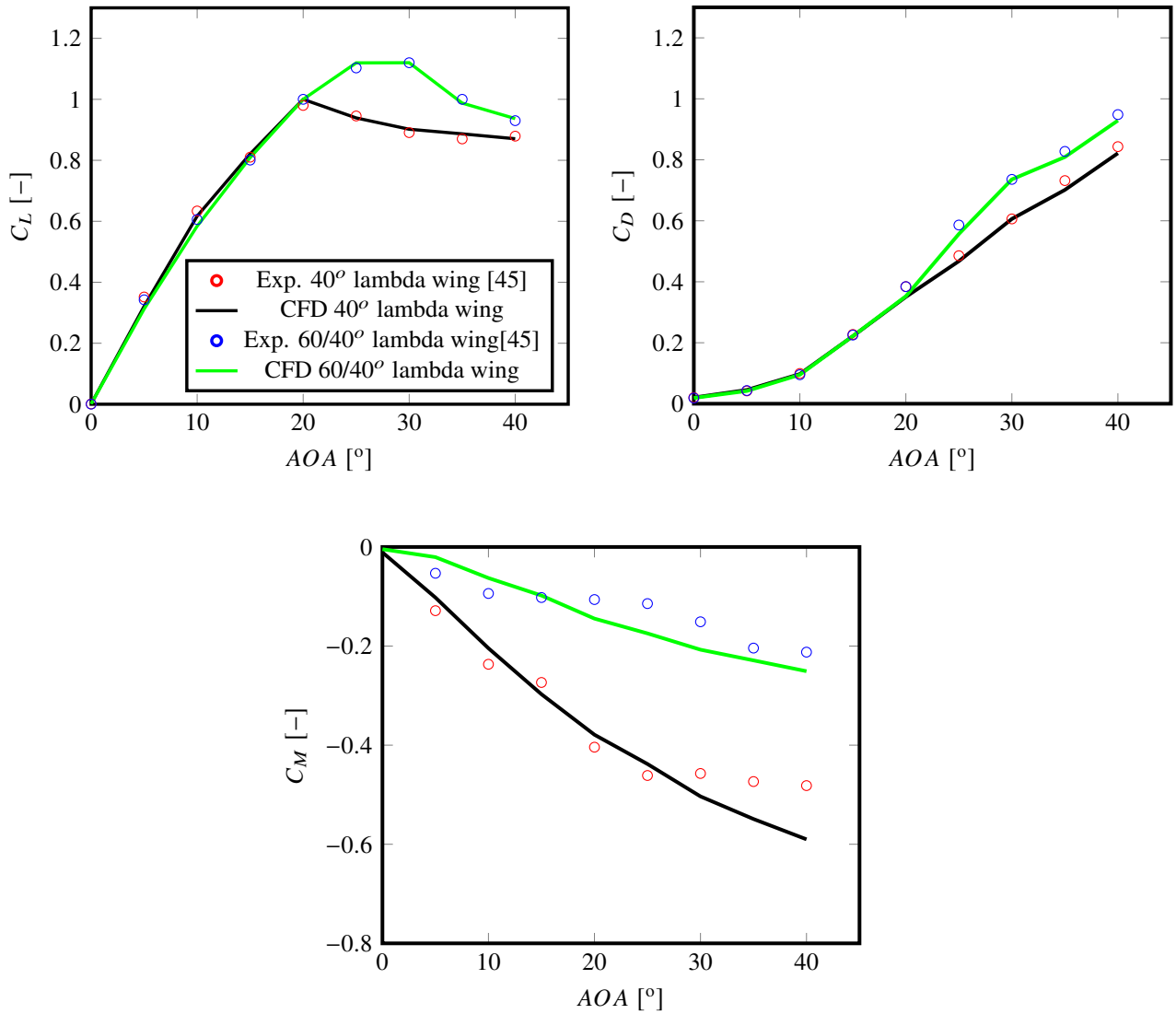

Fig. 9 Validation of CFD with experimental data.

C. Convergence Study, Residuals and Forces

Fig. 10 shows the evolution of the dimensionless lift and drag coefficients for 40° lambda and $60/40^o$ lambda wings at 25° AOA. The figure indicates that the C_L and C_D converge approximately after 1000 iterations for both lambda wing models. However, the total number of iterations was fixed as 4000 to minimize the iterative convergence error.

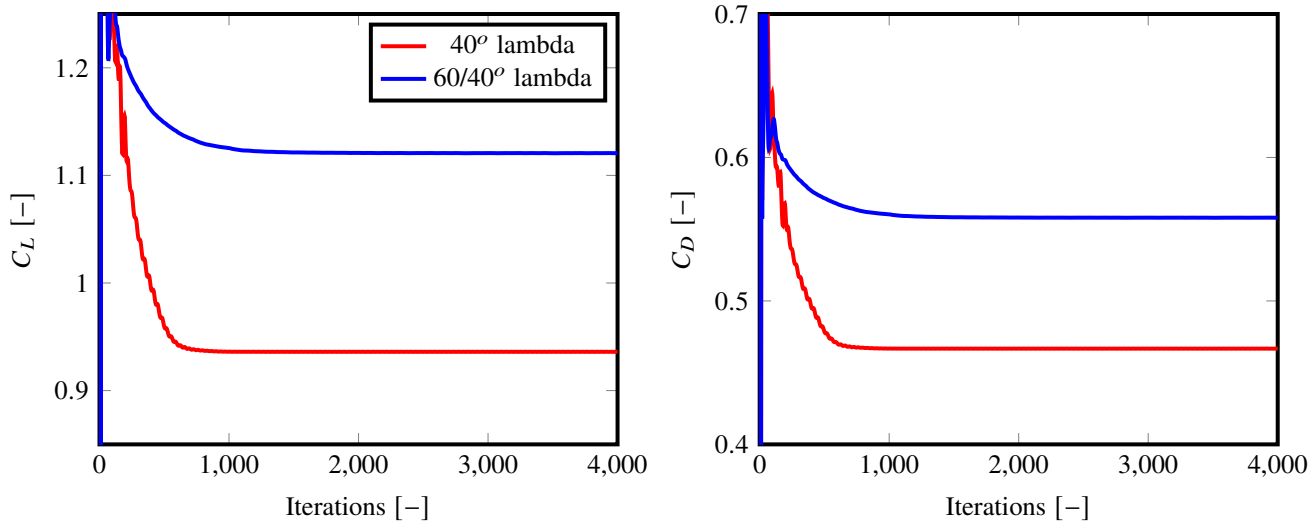

Fig. 10 Evolution of C_L and C_D values for 40° lambda and 60/40° lambda wings at AOA = 25°.

Furthermore, to ensure simulation convergence, residuals of pressure, velocity, turbulence kinetic energy, and specific turbulence dissipation rate are monitored and reported for the AOA at 25°. According to the ASME Journal of Fluids Engineering, a convergence criteria value lower than 10^{-4} was recommended [67], and the present simulations use a residual convergence value of 10^{-6}. The evolution of residuals for the 40° and 60/40° lambda wing models at 25° AOA are shown in Fig.11. As indicated in the figure, after 1000 iterations at 25° AOA, the residual of all variables falls below 10^{-4}. Due to altered flow behavior such as flow separation vortex breakdown, the residuals take longer to converge with the increase in AOA.

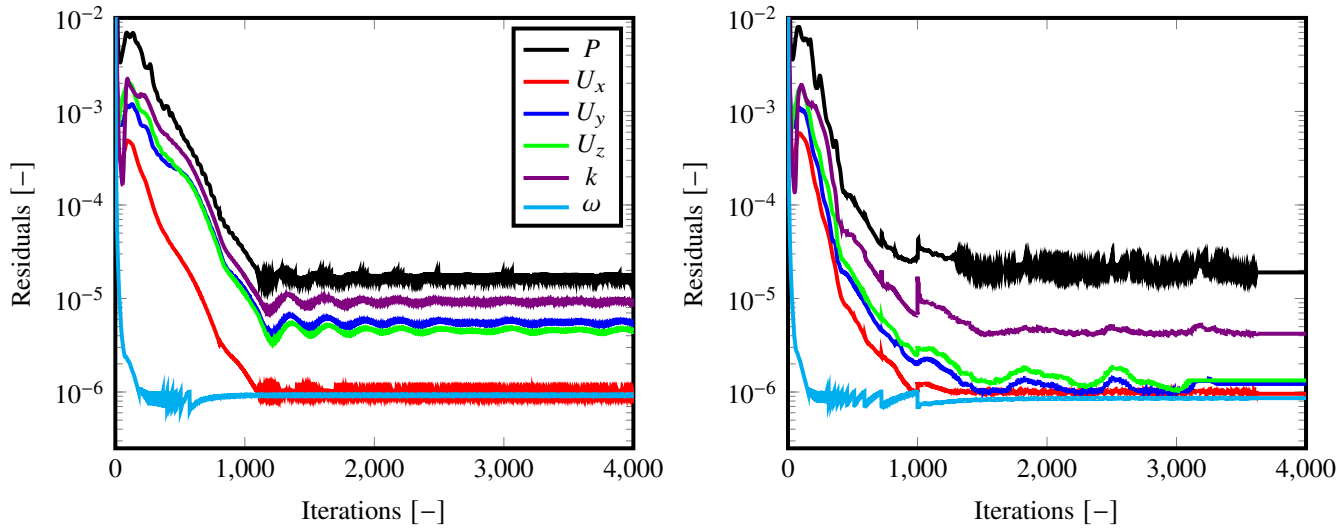

Fig. 11 Evolution of residuals for 40° lambda (left) and 60/40° lambda (right) wings at AOA = 25°.

D. Flowfield Analyses

Comparisons of the (C_p) distribution at three chordwise stations for various AOA values are shown in Fig.12 , Fig.13 and Fig.14. The selected AOA (10°, 15°, 20°, and 25°) represent moderate to high values. At 10 to 20° AOA, the 40° lambda wing is subjected to higher LE suction peaks. In contrast, the loading of the 60/40° lambda wing is less than the 40^olambda wing, which explains the reduced lift as shown in Fig. 9. However, at 25° AOA, the suction peak vanishes for the 40° lambda wing, which indicates flow separation. In contrast, for the 60/40° lambda wing, the LE suction gradually increases with AOA, and the vortex breakdown is delayed.

The SS pressure coefficient contours from 0 to 40° AOA are shown in Fig. 15 and 16 to understand the evolution of flow topology and vortex core locations with increasing AOA. The pressure contours show that high pressure occurs over most SS at AOA = 0° and a moderate degree of the low-pressure areas over LE regions at 5° AOA. As AOA increases, the primary vortices are generated from the rolling up of shear layer along the LE. The apex and primary vortices emerge more prominently as AOA increases, and the vortices cores are visible through the low-pressure regions at AOA = 10°. The negative pressure area results in vortices that emerge from the wing tip and apex, thereby increasing the lift force. For AOA=15°, due to the increasing unfavorable pressure gradient, the initiation point of the outboard vortex shifts in the direction of the wing apex. Likewise, the outboard portion of the vortices follows the wing chordwise direction and aligns with the free-stream flow, reducing lift on the outboard section.

With a further increase in AOA, the region along the spanwise axis where this re-alignment takes place shifts further inboard, and the vortices align with the TEs, further decreasing lift on the wing's back. As a powerful apex vortex emerges, the lift close to the nose begins to rise. Furthermore, the 40° lambda wing exhibits reduced LE suction for AOA > 20°, whereas the strength of LE suction is relatively higher for the 60/40° case for higher AOA values due to the influence of non-constant LE sweep angle. The higher suction implies highly energized vortices, and it delays stall inception and enhances aerodynamic performance.

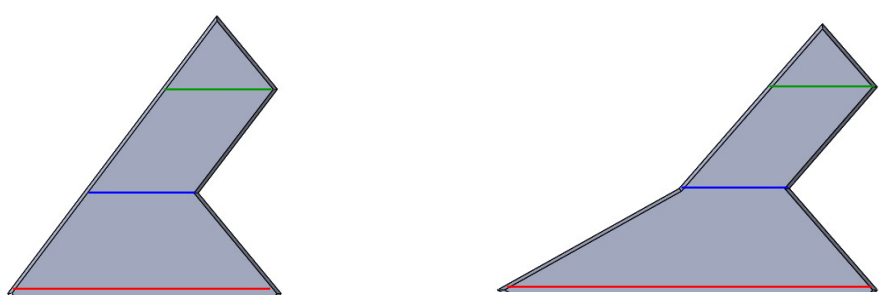

Fig. 12 Location of slices for pressure distribution for the 40° (left) and 60/40° (right) lambda wings.

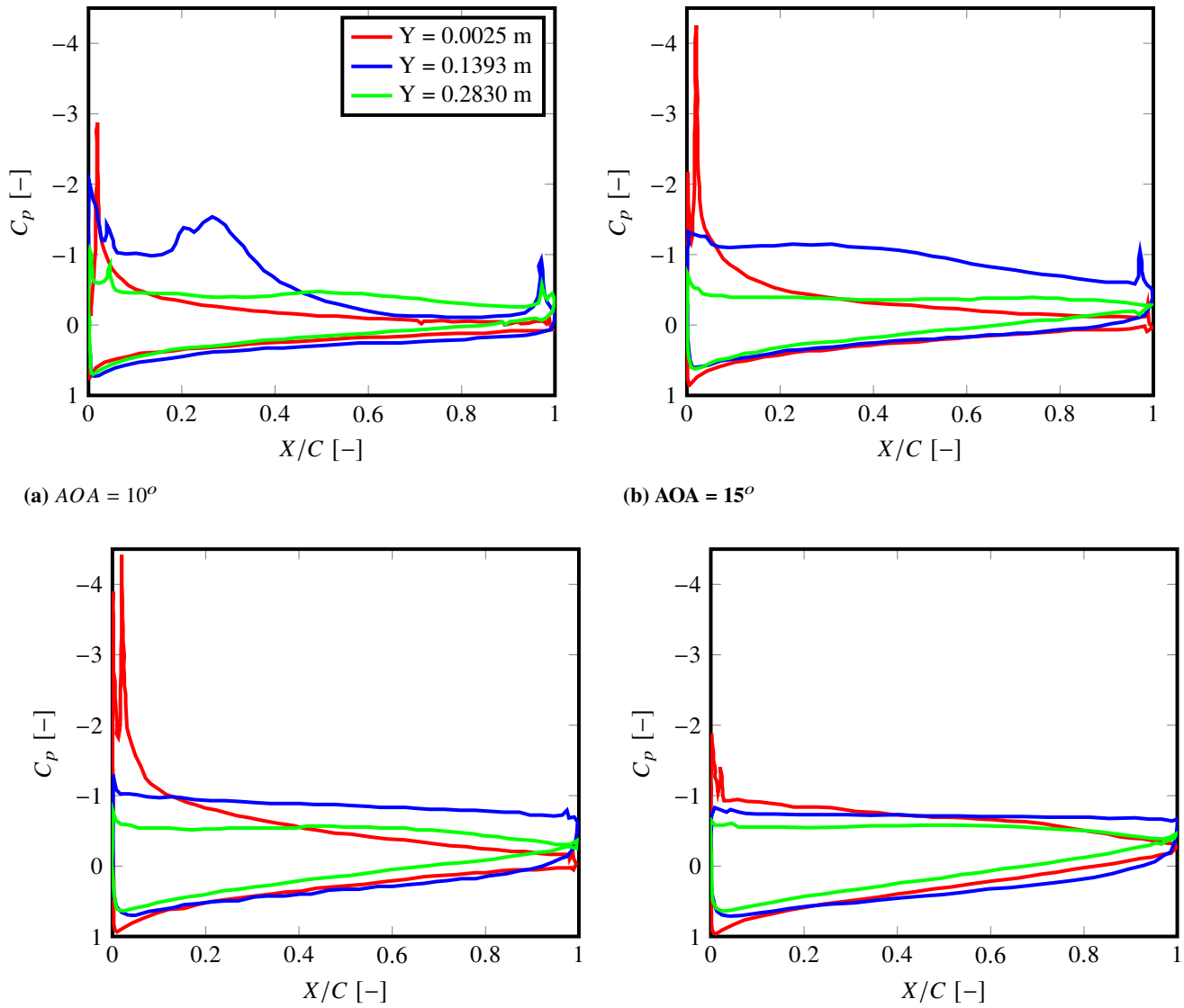

(a) $AOA = 10^o$

(b) AOA = 15°

(c) AOA = 20°

(d) AOA = 25°

Fig. 13 C_p **distribution for the 40° lambda wing at various Y locations.**

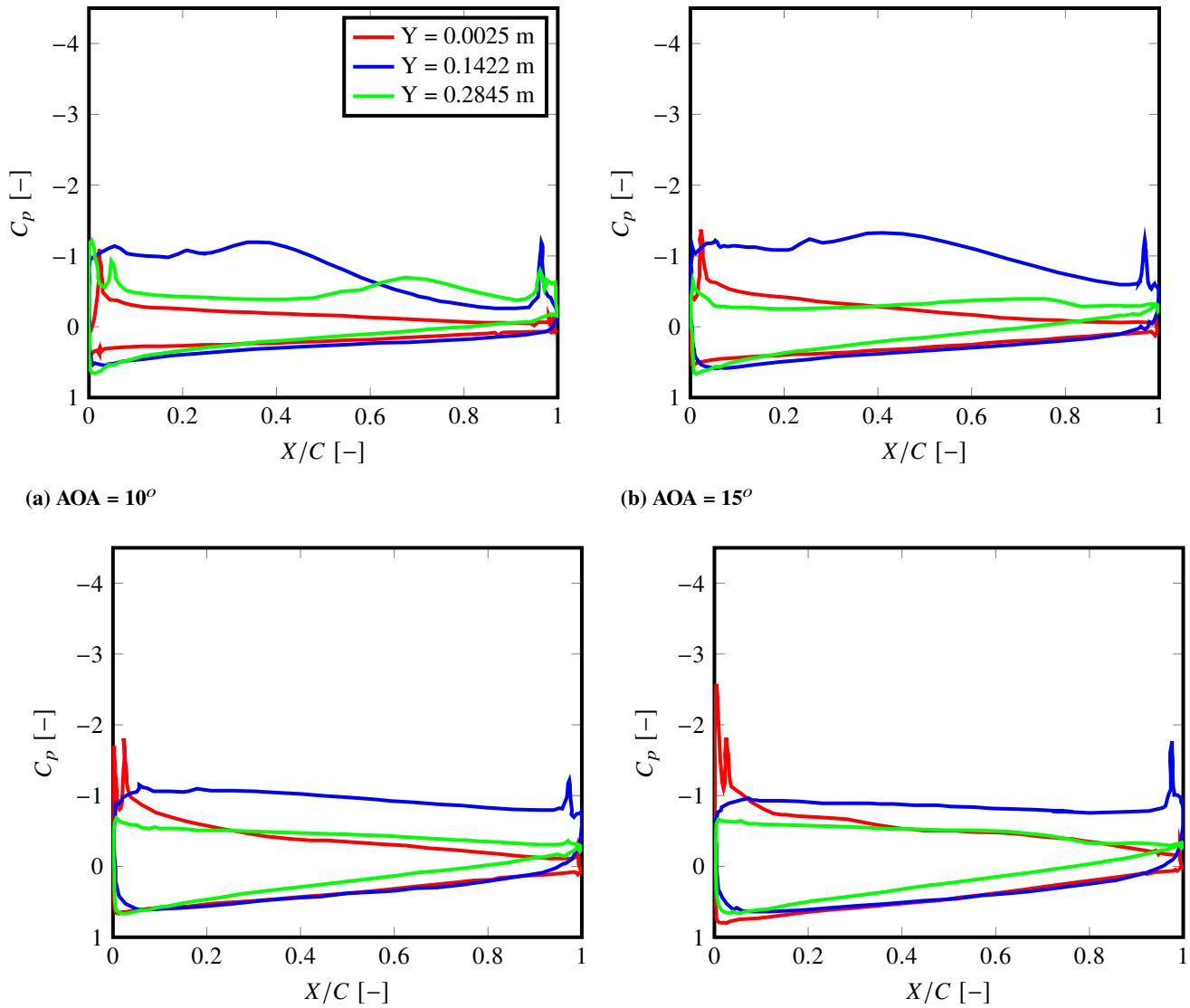

(a) AOA = 10°

(b) AOA = 15°

(c) AOA = 20°

(d) AOA = 25°

Fig. 14 C_p distribution for the 40/60° lambda wing at various Y locations.

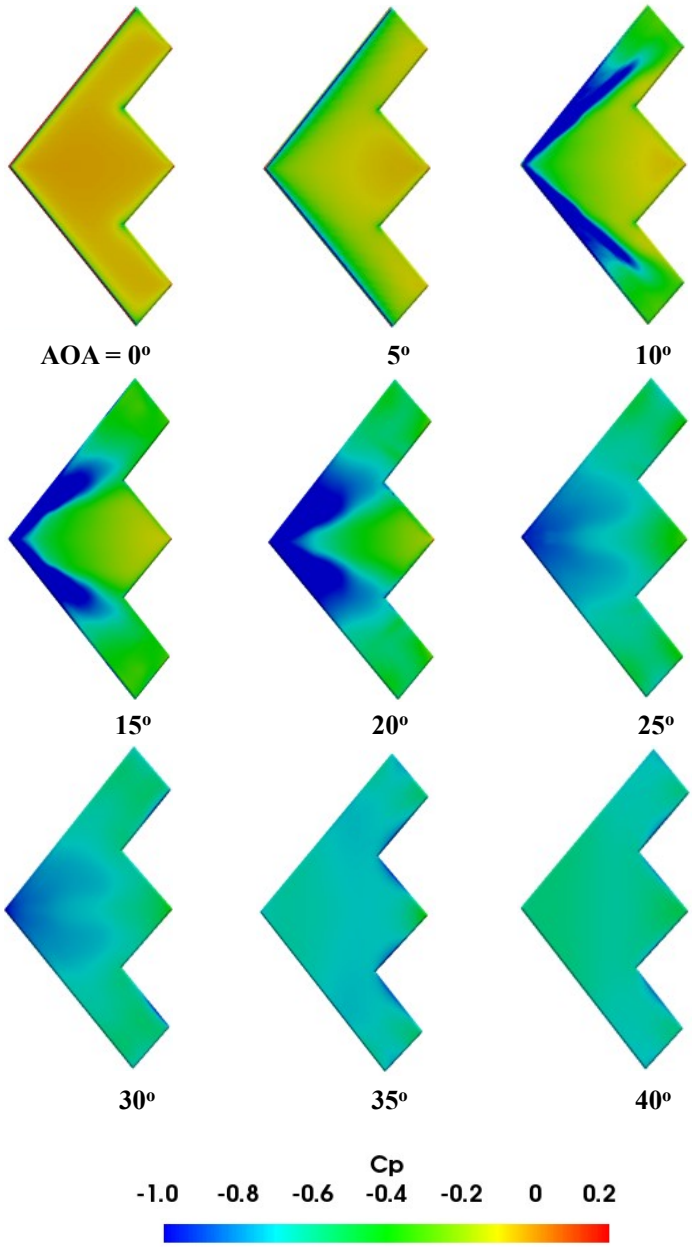

Fig. 15 C_p **distribution for the 40° at various AOA.**

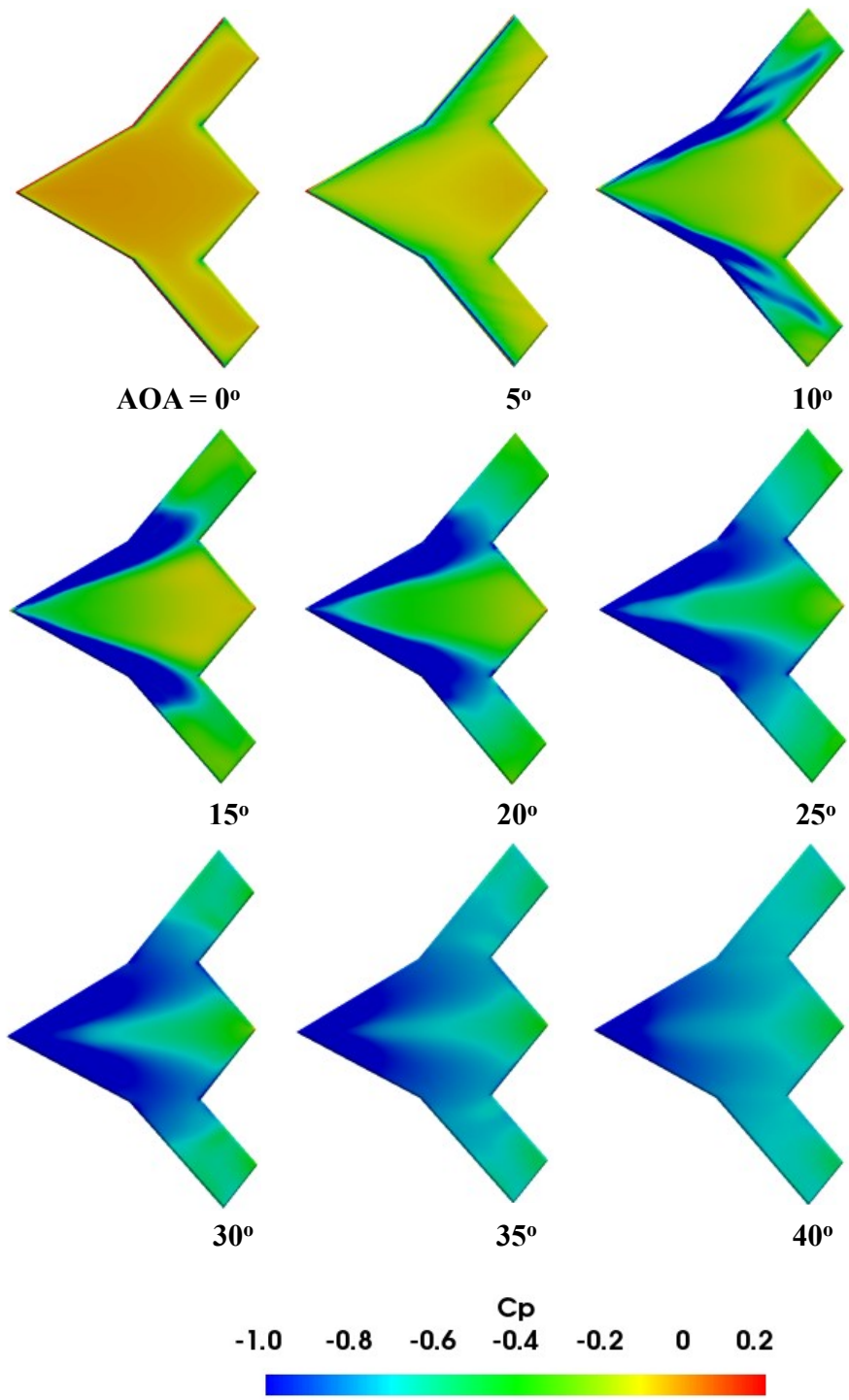

Fig. 16 C_p **distribution for the 60/40° at various AOA.**

To further understand the influence of pressure distribution between the 40° and 60/40° lambda wing for AOA >20°, the flow streamlines at various planes along the spanwise direction are provided in Fig.17. For both configurations, the flow separation originates from the outboard and moves toward the inboard region and the size of the recirculation

region increases with AOA. For AOA 30°, flow recirculation is visible on the outboard section, whereas the flow is attached on the symmetry plane for both cases. For AOA = 35°, a large recirculation region is visible at the symmetry plane for the 40° lambda wing case, and in contrast, the 60/40° lambda wing exhibits attached flow.

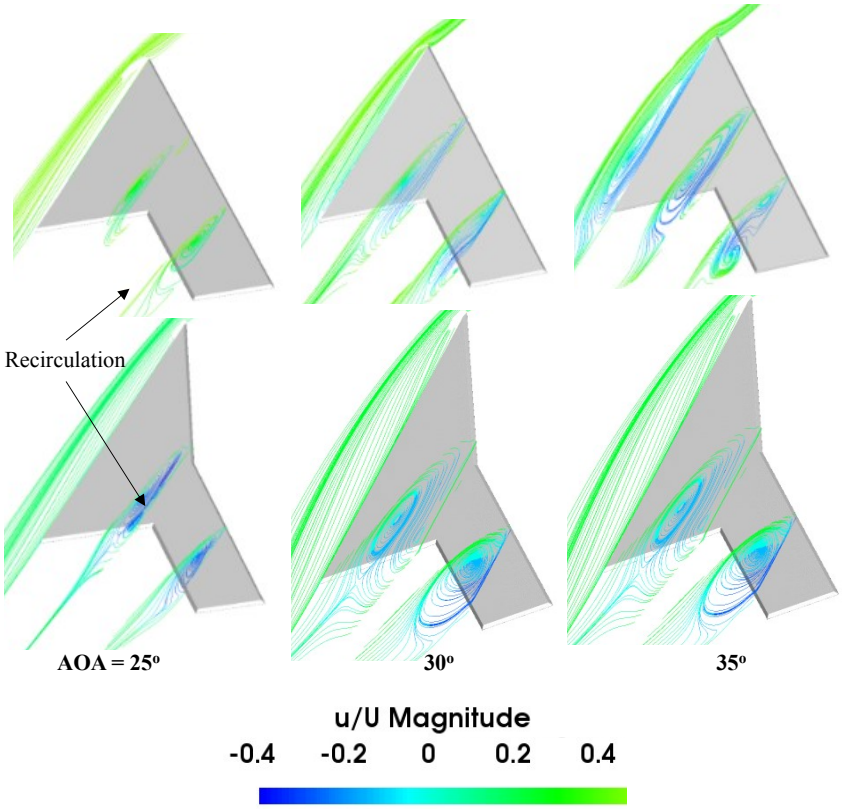

Fig. 17 Streamlines at various spanwise planes for the 40° lambda (top) and 60/40° lambda (bottom) wings.

To comprehend the flow behavior of the wing models, the flow structure was visualized using C_p and wall shear streamlines to describe the flow progression, attachment, detachment, and vortex breakdown with increasing AOA (Fig.18). For all cases, a vortex formation is observed at the wing apex, and the vortical flow expands as it moves downstream, and it weakens with the increase in AOA due to the rise in pressure. The increased radius of the streamlined rotational path implies an expanded vortex core. Also, the breakdown region shifts upstream and gradually stretches as the AOA increases. On the other hand, the local AOA at LE decreases with an increase in LE sweep angle; as a result, the higher sweep angle wings exhibit delayed stall compared to the low sweep angle wings [39]. Additionally, the figure shows that the vortex breakdown occurs for the 40° lambda wing.

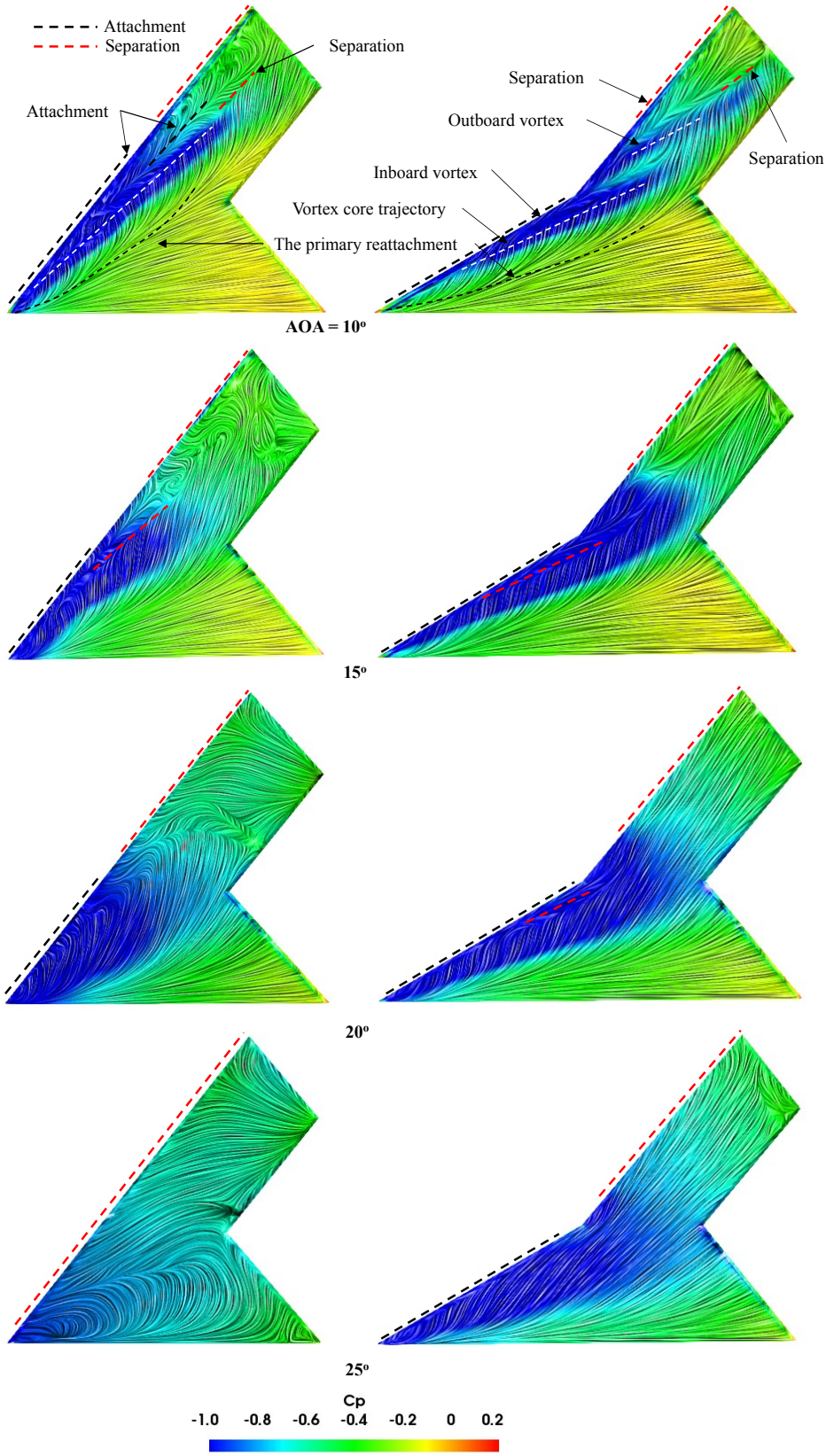

Fig. 18 Cp **contour with wall shear streamlines for the 40° (left) and 60/40° (right) lambda wing.**

In contrast, the significant flow characteristics over the 60/40° lambda wing are the existence, interaction, coiling-up, merging, and vortex breakdown development of two distinct LE separation vortices originating from the inboard and outboard LEs, which form and remain separate at low AOA. The inboard vortex (IBV) is adequately strong to recirculate the flow at higher AOA, while the strength of the outboard vortex (OBV) reduces at higher AOA. The AOA and inboard and outboard LEs sweep angles affect the interaction development and breakdown of IBV and OBV. The Cp distribution over wing SS exhibits pair of vortices with high suction at their cores at AOA = 10°, as shown in (Fig.18). The IBV and OBV interaction increased as AOA increased because of the increase in their sizes and strengths. Consequently, the OBV shifted inward whereas the IBV shifted outward, covering a large wing area. The lateral velocity generated by the IBV energizes the OBV and increases its local strength. As the AOA is further increased, the length of the merging zone reduces. At 15° AOA, the two vortices merge into a single vortex. Along the downstream kink of wing LE, the IBV is cut off from the inboard LE vorticity, and its strength reduces because of the viscous effects. Furthermore, the suction is higher at the apex region and reduces along the chordwise direction as the vortices lose their strength as they move downstream towards the TE. The strength and suction of OBV decreases, and it breaks down for AOA larger than 15°. In contrast, the strength and suction of IBV increases, and it breakdown for AOA greater than 25°.

Fig. 19 displays the vortical structures on SS visualized using the iso-surface Lambda 2 criterion (=25000). It can be seen that, for both cases, the primary vortex separates from the LE on the wing outboard, and the separation point shifts further upstream with the increase in AOA. The separated vortex that has less intensity grows in size and moves toward the inboard direction, as AOA increases. As discussed earlier, the flow behavior is identical for both cases for AOA 20°. A low momentum zone is visible near the outboard region, which increases in size and shifts towards the center plane as AOA increases.

For AOA = 25°, the low-velocity region completely engulfs the SS of the 40° lambda wing as the flow separation expands to the center plane, whereas for the 60/40° lambda wing, flow is attached at the center plane, and it has a higher velocity near the LE of strake due to increased suction. This behavior highlights the positive influence of the non-constant LE sweep angle which aids in delayed stall inception at higher AOA compared to the constant LE sweep angle case.

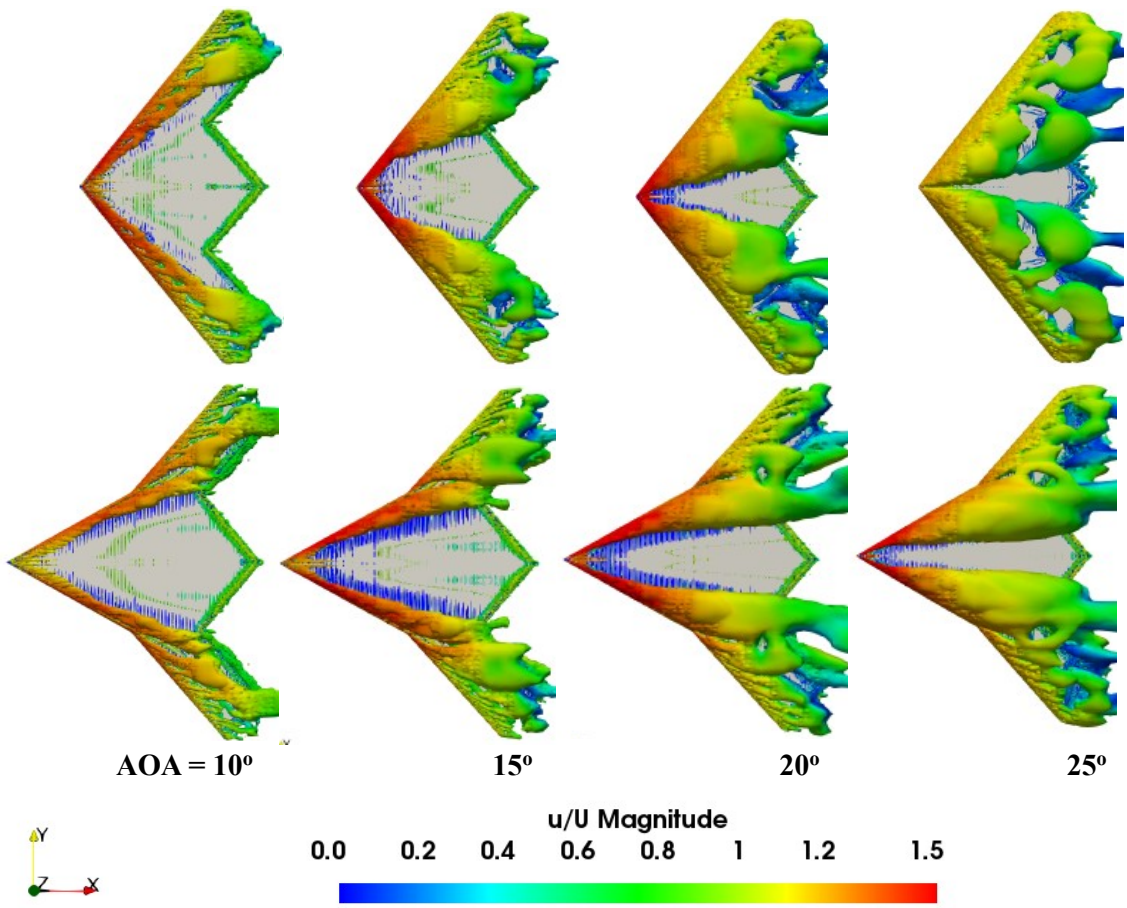

Fig. 19 Iso-surface of Lambda 2 criterion (=25000) on SS for the 40° (top) and 60/40° (bottom) lambda wings.

V. Conclusion

The LE sweep angle is a critical parameter that affects the aerodynamic performance of the UCAVs. The present study compares the vortical flow behavior of moderate (40°) and combined high-moderate (60/40°) sweep angle wing configurations. The aerodynamic performance of the two generic UCAV lambda wing models was investigated for various AOA. The numerical simulations were performed using OpenFOAM 8.0, and the numerical results have been validated against the experimental data. The present computational results matched well with the available experimental data.

With the increase in AOA, the pressure drop increased at the vortex core up to a critical AOA. The flow detachment originating on the wing outboard gradually shifted towards the wing inboard. The analyses of wall shear streamlines showed that the vortex flow moved inboard and became stronger and wider with increasing AOA. The vortex breakdown at the critical AOA and stall occurred. The wing model with a constant LE sweep angle of 40° showed increased LE vortex strength and the vortex breakdown at a relatively lower AOA value (>20°); alternatively, the wing with a non-constant LE sweep angle of 60/40° exhibited stable vortex and delayed stall.

On the basis of the present computational study, future research is planned to investigate the aerodynamic characteristics of a conceptual design and aerodynamic design optimization of UCAV configuration with a non-constant LE sweep angle to enhance the aerodynamic performance.

Acknowledgments

The authors would like to acknowledge NATO STO Support Project AVT-SP-002 Turbulence and the Aerodynamic Optimization of Nonplanar Lifting Systems.

References

[1] Wilson Jr, H. A., and Lovell, J. C., "Full-scale investigation of the maximum lift and flow characteristics of an airplane having approximately triangular plan form," Tech. rep., 1947. https://doi.org/https://ntrs.nasa.gov/citations/19930085702.

[2] Haines, A., "Some notes on the flow patterns observed over various swept-back wings at low Mach numbers (in the RAE 10-ft x 7-ft high speed tunnel)," 1954. https://doi.org/https://reports.aerade.cranfield.ac.uk/handle/1826.2/3761.

[3] Lambourne, N., and Bryer, D., "Some measurements in the vortex flow generated by a sharp leading edge having 65 degrees sweep," 1960. https://doi.org/https://reports.aerade.cranfield.ac.uk/handle/1826.2/490.

[4] Lambourne, N., and Bryer, D., "The bursting of leading-edge vortices-some observations and discussion of the phenomenon," 1961. https://doi.org/https://reports.aerade.cranfield.ac.uk/handle/1826.2/3859.

[5] Earnshaw, P., "An experimental investigation of the structure of a leading-edge vortex," 1961. https://doi.org/https://reports.aerade.cranfield.ac.uk/handle/1826.2/3858.

[6] Earnshaw, P., and Lawford, J., "Low-speed wind-tunnel experiments on a series of sharp-edged delta wings," 1964. https://doi.org/https://reports.aerade.cranfield.ac.uk/handle/1826.2/4008.

[7] Earnshaw, P. B., "Measurements of vortex-breakdown position at low speed on a series of sharp-edged symmetrical models," 1965. https://doi.org/https://reports.aerade.cranfield.ac.uk/handle/1826.2/841.

[8] Polhamus, E. C., "Predictions of vortex-lift characteristics by a leading-edge suctionanalogy," *Journal of aircraft*, Vol. 8, No. 4, 1971, pp. 193–199. https://doi.org/https://doi.org/10.2514/3.44254.

[9] Tobak, M., and Peake, D. J., "Topology of three-dimensional separated flows," *Annual review of fluid mechanics*, Vol. 14, No. 1, 1982, pp. 61–85. https://doi.org/https://doi.org/10.1146/annurev.fl.14.010182.000425.

[10] Delery, J. M., "Physics of vortical flows," *Journal of Aircraft*, Vol. 29, No. 5, 1992, pp. 856–876. https://doi.org/https://doi.org/10.2514/3.46256.

[11] Délery, J. M., "Robert Legendre and Henri Werlé: toward the elucidation of three-dimensional separation," *Annual review of fluid mechanics*, Vol. 33, 2001, p. 129. https://doi.org/https://doi.org/10.1146/annurev.fluid.33.1.129.

[12] Mitchell, A. M., Morton, S. A., Forsythe, J. R., and Cummings, R. M., "Analysis of delta-wing vortical substructures using detached-eddy simulation," *AIAA journal*, Vol. 44, No. 5, 2006, pp. 964–972. https://doi.org/https://doi.org/10.2514/1.755.

[13] Ol, M. V., and Gharib, M., "Leading-edge vortex structure of nonslender delta wings at low Reynolds number," *AIAA journal*, Vol. 41, No. 1, 2003, pp. 16–26. https://doi.org/https://doi.org/10.2514/2.1930.

[14] Gordnier, R., and Visbal, M., "Higher-order compact difference scheme applied to low sweep delta wing flow," *41st Aerospace Sciences Meeting and Exhibit*, 2003, p. 620. https://doi.org/https://doi.org/10.2514/6.2003-620.

[15] Yaniktepe, B., and Rockwell, D., "Flow structure on a delta wing of low sweep angle," *AIAA journal*, Vol. 42, No. 3, 2004, pp. 513–523. https://doi.org/https://doi.org/10.2514/1.1207.

[16] Gursul, I., Gordnier, R., and Visbal, M., "Unsteady aerodynamics of nonslender delta wings," *Progress in Aerospace Sciences*, Vol. 41, No. 7, 2005, pp. 515–557. https://doi.org/https://doi.org/10.1016/j.paerosci.2005.09.002.

[17] Verhaagen, N., and Elsayed, M., "Effects of Leading-Edge Shape on the Flow Over 50-deg Delta Wings," 26th *AIAA applied aerodynamics conference*, 2008, p. 7330. https://doi.org/https://doi.org/10.2514/6.2008-7330.

[18] Luckring, J., "A survey of factors affecting blunt-leading-edge separation for swept and semi-slender wings," 28th *AIAA applied aerodynamics conference*, 2010, p. 4820. https://doi.org/https://doi.org/10.2514/6.2010-4820.

[19] Defense, D., "Unmanned aircraft systems roadmap 2005–2030," Tech. rep., Tech. rep., August, 2005. https://doi.org/https://rosap.ntl.bts.gov/view/dot/18248.

[20] McParlin, S., Bruce, R., Hepworth, A., and Rae, A., "Low speed wind tunnel tests on the 1303 UCAV concept," 24th *AIAA Applied Aerodynamics Conference*, 2006, p. 2985. https://doi.org/https://doi.org/10.2514/6.2006-2985.

[21] Petterson, K., "CFD analysis of the low-speed aerodynamic characteristics of a UCAV," 44th *AIAA Aerospace Sciences Meeting and Exhibit*, 2006, p. 1259. https://doi.org/https://doi.org/10.2514/6.2006-1259.

[22] Petterson, K., "Low-speed aerodynamic and flowfield characteristics of a UCAV," 24th *Applied Aerodynamics Conference. San Francisco, California 5-8 June*, AIAA Paper 2006-2986. https://doi.org/https://doi.org/10.2514/6.2006-2986.

[23] Woolvin, S., "UCAV configuration & performance trade-offs," 44th *AIAA Aerospace Sciences Meeting and Exhibit, Reno, Nevada, 09 - 12 January, 2006*, AIAA Paper 2006-1264, p. 1264. https://doi.org/https://doi.org/10.2514/6.2006-1264.

[24] Shim, H., and Park, S. O., "Low-speed wind-tunnel test results of a BWB-UCAV model," *Procedia Engineering*, Vol. 67, 2013, pp. 50–58. https://doi.org/https://doi.org/10.1016/j.proeng.2013.12.004.

[25] Coppin, J., "Aerodynamics, stability and shape optimisation of unmanned combat air vehicles," Ph.D. thesis, University of Sheffield, 2014. https://doi.org/https://etheses.whiterose.ac.uk/6987/1/thesis-Joe-Coppin.pdf.

[26] Cummings, R., and Schuette, A., "An integrated computational/experimental approach to UCAV stability & control estimation: overview of NATO RTO AVT-161," 28th *AIAA Applied Aerodynamics Conference*, 2010, p. 4392. https://doi.org/https://doi.org/10.2514/6.2010-4392.

[27] Konrath, R., Roosenboom, E., Schröder, A., Pallek, D., and Otter, D., "Static and dynamic SACCON PIV tests, part II: aft flow field," 28th *AIAA applied aerodynamics conference*, 2010, p. 4396. https://doi.org/https://doi.org/10.2514/6.2010-4396.

[28] Loeser, T., Vicroy, D., and Schütte, A., "SACCON static wind tunnel tests at DNW-NWB and 14 x22 NASA LaRC," $28^{t}h$ *AIAA applied aerodynamics conference, Chicago, Illinois, 28 June 2010 - 01 July 2010*, AIAA Paper 2010-4393, p. 4393. https://doi.org/https://doi.org/10.2514/6.2010-4393.

[29] Vicroy, D., Loeser, T., and Schütte, A., "SACCON dynamic wind tunnel tests at DNW-NWB and 14´ x22´ NASA LaRC," 28th *AIAA Applied Aerodynamics Conference, 2010*, AIAA Paper 2010-4394, p. 4394. https://doi.org/https://doi.org/10.2514/6.2010-4394.

[30] Cummings, R. M., and Schütte, A., "Integrated computational/experimental approach to unmanned combat air vehicle stability and control estimation," *Journal of Aircraft*, Vol. 49, No. 6, 2012, pp. 1542–1557.

[31] Yayla, S., Canpolat, C., Sahin, B., and Akilli, H., "The effect of angle of attack on the flow structure over the nonslender lambda wing," *Aerospace Science and Technology*, Vol. 28, No. 1, 2013, pp. 417–430. https://doi.org/https://doi.org/10.1016/j.ast.2012.12.007.

[32] Schütte, A., Huber, K. C., and Boelens, O. J., "Static and dynamic numerical simulations of a generic UCAV configuration with and without control devices," 32nd *AIAA Applied Aerodynamics Conference*, 2014, p. 2132.

[33] Liersch, C. M., Huber, K. C., Schütte, A., Zimper, D., and Siggel, M., "Multidisciplinary design and aerodynamic assessment of an agile and highly swept aircraft configuration," *CEAS Aeronautical Journal*, Vol. 7, 2016, pp. 677–694.

[34] Nangia, R. K., Coppin, J., and Ghoreyshi, M., "A UCAV Wing Design, Assessment and Comparisons." *2018 Applied Aerodynamics Conference, Atlanta, Georgia, 25-29 June, 2018*, AIAA Paper 2018-2842, p. 2842. https://doi.org/https://doi.org/10.2514/6.2018-2842.

[35] Liersch, C. M., Cummings, R., Schütte, A., et al., "NATO STO/AVT-251: A Joint Exercise in Collaborative Combat Aircraft Design," *NATO STO Review*, 2022. https://doi.org/https://review.sto.nato.int/index.php/journal-issues/spring-2022/avt-324/39-a-joint-exercise-in-collaborative-combat-aircraft-design.

[36] Liersch, C. M., and Bishop, G., "Conceptual design of a 53 deg swept flying wing UCAV configuration," *2018 Applied Aerodynamics Conference, Atlanta, Georgia, June 25-29, 2018*, AIAA Paper 2018-2839, p. 2839. https://doi.org/https://doi.org/10.2514/6.2018-2839.

[37] SchütteSch, A., Vormweg, J., Maye, R. G., and Jeans, T., "Aerodynamic shaping design and vortical flow design aspects of a 53 deg swept flying wing configuration," *2018 Applied Aerodynamics Conference, Atlanta, Georgia, June 25-29, 2018*, AIAA Paper 2018-2841, p. 2841. https://doi.org/https://doi.org/10.2514/6.2018-2841.

[38] Cummings, R. M., Liersch, C., and Schuette, A., "Multi-disciplinary design and performance assessment of effective, agile NATO air vehicles," *2018 Applied Aerodynamics Conference, Atlanta, Georgia, June 25-29, 2018*, AIAA Paper 2014-2838, June 2018, p. 2838. https://doi.org/https://doi.org/10.2514/6.2018-2838.

[39] Brett, J., and Ooi, A., "Effect of sweep angle on the vortical flow over delta wings at an angle of attack of 10," *Journal of Engineering Science and Technology*, Vol. 9, No. 6, 2014, pp. 768–781. https://doi.org/https://jestec.taylors.edu.my/Vol.

[40] Luckring, J. M., and Boelens, O. J., "A unit-problem investigation of blunt leading-edge separation motivated by AVT-161 SACCON research," *NATO RTO Specialists Meeting AVT-189*, 2011. https://doi.org/https://ntrs.nasa.gov/citations/20110016428.

[41] Luckring, J. M., and Boelens, O. J., "A reduced-complexity investigation of blunt leading-edge separation motivated by UCAV aerodynamics," *53rd AIAA Aerospace Sciences Meeting*, 2015, p. 0061.

[42] Manshadi, M. D., Eilbeigi, M., Sobhani, M. K., Zadeh, M. B., and Vaziry, M. A., "Experimental study of flow field distribution over a generic cranked double delta wing," *Chinese Journal of Aeronautics*, Vol. 29, No. 5, 2016, pp. 1196–1204. https://doi.org/https://doi.org/10.1016/j.cja.2016.08.002.

[43] Yaniktepe, B., ÖZalp, C., and Canpolat, Ç., "Aerodynamics and flow characteristics of X-45 delta wing planform," *Kahramanmaraş Sütçü İmam Üniversitesi Mühendislik Bilimleri Dergisi*, Vol. 19, No. 1, 2016, pp. 1–10. https://doi.org/http://jes.ksu.edu.tr/tr/download/article-file/181023.

[44] Schütte, A., Hummel, D., and Hitzel, S. M., "Flow Physics Analyses of a Generic Unmanned Combat Aerial Vehicle Configuration," *Journal of Aircraft*, Vol. 49, 2012, pp. 1638–1651. https://doi.org/https://doi.org/10.2514/1.C031386.

[45] Ali, U., Chadwick, E., et al., "Flow control and high-lift performance for flying-wing manned Combat Air Vehicle Configurations by inserting lots," *The International Journal of Multiphysics*, Vol. 10, No. 2, 2016. https://doi.org/http://dx.doi.org/10.21152/1750-9548.10.2.117.

[46] Löchert, P., Huber, K. C., and Rütten, M., *Control concepts for an agile and highly swept flying wing configuration*, Deutsche Gesellschaft für Luft-und Raumfahrt-Lilienthal-Oberth eV, 2018.

[47] Ganglin, W., "Key parameters and conceptual configuration of unmanned combat aerial vehicle concept," *Chinese Journal of Aeronautics*, Vol. 22, No. 4, 2009, pp. 393–400. https://doi.org/https://doi.org/10.1016/S1000-9361(08)60116-8.

[48] "solidworks," https://www.solidworks.com/, 2020.

[49] "openfoam," https://www.openfoam.com/, 2020.

[50] Greenshields, C. J., "OpenFOAM user guide Version 8," *The OpenFOAM Foundation*, Vol. 237, 2020.

[51] "salome," https://www.salome-platform.org/, 2019.

[52] Ashton, N., Unterlechner, P., and Blacha, T., "Assessing the sensitivity of hybrid RANS-LES simulations to mesh resolution, numerical schemes and turbulence modelling within an industrial CFD process," Tech. rep., SAE Technical Paper, 2018. https://doi.org/https://doi.org/10.4271/2018-01-0709.

[53] Yavuz, M., "Investigation of flow characteristics and vortex formations of lambda wing at high angles of attack," *Journal of Thermal Engineering*, Vol. 6, No. 6, 2020, pp. 282–297. https://doi.org/10.18186/thermal.829872.

[54] Elkhoury, M., *Aerodynamics of unmanned combat air vehicles: flow structure and control*, Lehigh University, 2004.

[55] Yaniktepe, B., and Rockwell, D., "Flow structure on diamond and lambda planforms: Trailing-edge region," *AIAA journal*, Vol. 43, No. 7, 2005, pp. 1490–1500.

[56] Yavuz, M. M., "Numerical analysis of vortex breakdown of unmanned combat air vehicles," Ph.D. thesis, M. Sc. Dissertation, Mechanical Engineering Dept. Adana: Cukurova University, 2011.

[57] Wibowo, S. B., Rohmat, T. A., et al., "An evaluation of turbulence model for vortex breakdown detection over delta wing," *Archive of Mechanical Engineering*, Vol. 65, No. 3, 2018. URL http://journals.pan.pl/Content/108631/PDF/AME_124489.pdf.

[58] Le Moigne, Y., and Rizzi, A., "Grid Study for Euler Simulations of a 70 Delta Wing with the Unstructured Flow Solver Edge," *RTO Rep-084*, 2004.

[59] Al-Garni, A. Z., Saeed, F., and Al-Garni, A. M., "Experimental and numerical investigation of 65 degree Delta and 65/40 degree double-delta wings," *Journal of Aircraft*, Vol. 45, No. 1, 2008, pp. 71–76. https://doi.org/https://doi.org/10.2514/1.20243.

[60] Mi, B.-g., Zhan, H., and Chen, B.-b., "New systematic CFD methods to calculate static and single dynamic stability derivatives of aircraft," *Mathematical Problems in Engineering*, Vol. 2017, 2017.

[61] Stucke, J., "Vortex Development for a 65 swept back Delta Wing with Varying Thickness and Maximum Thickness Location," Ph.D. thesis, 2020.

[62] Kelayeh, R. K., and Djavareshkian, M. H., "Aerodynamic investigation of twist angle variation based on wing smarting for a flying wing," *Chinese Journal of Aeronautics*, Vol. 34, No. 2, 2021, pp. 201–216. https://doi.org/https://doi.org/10.1016/j.cja.2020.06.022.

[63] Kapsalis, S., Kantouros, B., Panagiotou, P., and Yakinthos, K., "A DOE-based method for the aerodynamic, stability and layout optimization of a tactical Blended-Wing-Body UAV," *AIAA SCITECH 2022 Forum*, 2022, p. 0127. https://doi.org/https://doi.org/10.2514/6.2022-0127.

[64] Celik, I. B., Ghia, U., Roache, P. J., and Freitas, C. J., "Procedure for estimation and reporting of uncertainty due to discretization in CFD applications," *Journal of fluids Engineering-Transactions of the ASME*, Vol. 130, No. 7, 2008.

[65] Manna, P., Dharavath, M., Sinha, P., and Chakraborty, D., "Optimization of a flight-worthy scramjet combustor through CFD," *Aerospace science and technology*, Vol. 27, No. 1, 2013, pp. 138–146. https://doi.org/https://doi.org/10.1016/j.ast.2012.07.005.

[66] Kumar, P. M., and Samad, A., "Nature-inspired design of a turbine blade harnessing wave energy," *Proceedings of the Institution of Mechanical Engineers, Part A: Journal of Power and Energy*, Vol. 234, No. 5, 2020, pp. 670–689. https://doi.org/https://doi.org/10.1177/0957650919874.

[67] Roache, P. J., Ghia, K. N., and White, F. M., "Editorial policy statement on the control of numerical accuracy," *Journal of Fluids Engineering*, Vol. 108, No. 1, 1986, p. 2. https://doi.org/https://doi.org/10.1115/1.3242537.